Highly Efficient Preparation of $Ce_{0.8}Sm_{0.2}O_{2-\delta}$–$SrCo_{0.9}Nb_{0.1}O_{3-\delta}$ Dual-phase Four-channel Hollow Fiber Membrane via One-step Thermal Processing Approach

Ke Ning[1,#], Zhicheng Zhang[1,#], Zhi Xu[1], Qiankun Zheng[1], Jingkun Tan[1], Zhengkun Liu[1], Zhentao Wu[2], Guangru Zhang[1,*] and Wanqin Jin[1]

1. State Key Laboratory of Materials-Oriented Chemical Engineering, College of Chemical Engineering, Nanjing Tech University, 30 Puzhu Road(S), Nanjing 211816, P.R. China
2. Aston Institute of Materials Research (AIMR), Aston University, B4 7ET, UK

# Ke Ning and Zhicheng Zhang contributed equally.

*Corresponding author: Guangru Zhang

Contact information:

AProf. Guangru Zhang

State Key Laboratory of Materials-Oriented Chemical Engineering, Nanjing Tech University, 30 Puzhu South Road, Nanjing 211816, P. R. China

Tel.: +86-25-83172266;

Fax: +86-25-83172272;

E-mail: Guangru.Zhang@njtech.edu.cn (AProf. Zhang)

Abstract

Fabricating dual-phase hollow-fiber membranes via a one-step thermal processing (OSTP) approach is challenging, because of complex sintering kinetics and the subsequent impacts on membrane morphology, phase stability, and permeation properties. In this study, we have demonstrated that $Ce_{0.8}Sm_{0.2}O_{2-\delta}$-$SrCo_{0.9}Nb_{0.1}O_{3-\delta}$ (SDC-SCN) four-channel hollow fiber membrane can be manufactured via a single high-temperature sintering process, by using metal oxides and carbonates directly as membrane materials (sources of metal ions). It has been found that use of a low ramping rate reduces grain sizes, increases grain and forming cobalt oxide nanoparticles, a key step to promoting surface exchange process followed by enhancing oxygen permeation. While the grain boundary interface region can be limited to approximately 20-30 nm. At 1173 K oxygen permeation of the SDC-SCN four-channel hollow fiber membrane was measured at approximately 1.2 $mL \cdot cm^{-2} \cdot min^{-1}$ using helium as the sweep gas. Meanwhile, the dual-phase membrane shows a good tolerance to carbon dioxide, with the oxygen permeation flux fully recovered after long-term exposure to carbon dioxide (more than 100 h). This will enable further application of the OSTP approach for preparing dual-phase multi-channel hollow fiber membranes for applications of oxyfuel combustion, catalytic membrane reactors and carbon dioxide capture.

Keywords: Dual-phase membrane; Multi-channel hollow fiber; One-step thermal processing; Sintering kinetics; CO_2-tolerance

1. Introduction

Mixed ionic-electronic conducting (MIEC) membranes, a type of high temperature oxygen perm-selective membranes enabling energy-efficient separation and various "green" chemistry opportunities, have garnered a lot of interests from industrial and academic communities over the past decades. The great selectivity to oxygen (theoretically 100%) at temperatures over 973 K allows effective separation of pure oxygen and complete rejection of other gaseous substances. After years of development, applications of MIEC oxygen-permeable membrane have been extended to areas other than air separation, such as membrane reactor for effective conversion of natural gas, hydrogen production and abatement of greenhouse gases [1-4]. Perovskite oxide (ABO_3) is one of the mostly studied MIEC materials. However, owing to the existence of active transition metals and alkali metals (such as Ba, Sr, CO, Cu, Fe, etc.), segregation of elements, unwanted reactions between gaseous molecules and membrane materials, and etching of membrane surface occur readily during long-term operation, which significantly restricts lifetime of membrane reactors under strongly reducing and/or corrosive atmospheres (e.g. hydrogen, carbon monoxide, hydrogen sulfide, carbon dioxide and sulfur dioxide)[5-7]. To address such issues, oxygen-permeable membranes consisting of a dual-phase material have been the focus of catalytic membrane reactor research, due to a more flexible design of membrane material and significantly improved thermal-chemical stability of the membranes. The dual-phase membranes normally consist of a perovskite oxide phase and a second fluorite oxide phase. Both oxides can conduct oxygen ions at high temperatures, forming continuous pathways for efficient transport of oxygen ions. Meanwhile, fluorite oxides are thermal-chemically very stable, inhibiting element segregation of perovskite oxides during oxygen permeation, thus improving membrane stability [8-15].

Different from conventional approaches which normally involve multiple material processing steps and sintering, oxides and carbonates were directly utilized as precursor membrane materials for the preparation of a dual-phase four-channel hollow fiber membrane via a one-step thermal processing (OSTP) approach. A composite of 60wt.%$Ce_{0.8}Sm_{0.2}O_{2-\delta}$-40wt.%$SrCo_{0.9}Nb_{0.1}O_{3-\delta}$ (SDC-SCN) was selected as the target phase of the membrane, due to its high oxygen permeability and carbon dioxide tolerance proved in our previous study [16]. Meanwhile, a multi-channel hollow fiber membrane geometry was selected due to its advantages in both oxygen permeation and mechanical robustness, when compared with alternative geometries such as disk-like membrane, tubular membrane and single-channel hollow fiber membrane [17-19].

The feasibility of the OSTP approach has been demonstrated in our previous study [20], where oxides or carbonates, instead of as-prepared perovskite oxides, were directly employed in a phase-inversion process for fabrication of a single-phase perovskite hollow fiber membrane. In this OSTP, solid-state reactions converting raw chemicals (metal ion sources) into perovskite oxides and membrane densification occurred simultaneously (**Fig.1a**), allowing approximately 50% reduction in time and energy required in conventional multi-step approaches [20]. To advance the OSTP approach to the preparation of dual-phase hollow fiber membranes, the biggest challenge is controlling and stabilizing crystal structures of separate oxides during the single thermal treatment, as the thermodynamics and kinetics of crystallization are commonly very different between perovskites and fluorites. As shown in **Fig. 1b and c**, any mismatch between crystallization (solid-state reaction) and densification (solid-state sintering) rates (i.e., (i) crystallization of perovskites; (ii) crystallization of fluorites; (iii) densification of perovskite phases; (iv) densification of fluorite phases and (v) co-densification of the two phases) leads to the formation of impurities and residues

(the two phases might be physically isolated by the formation impurity particles) and impair integrity and perm-selectivity of the resultant membranes.

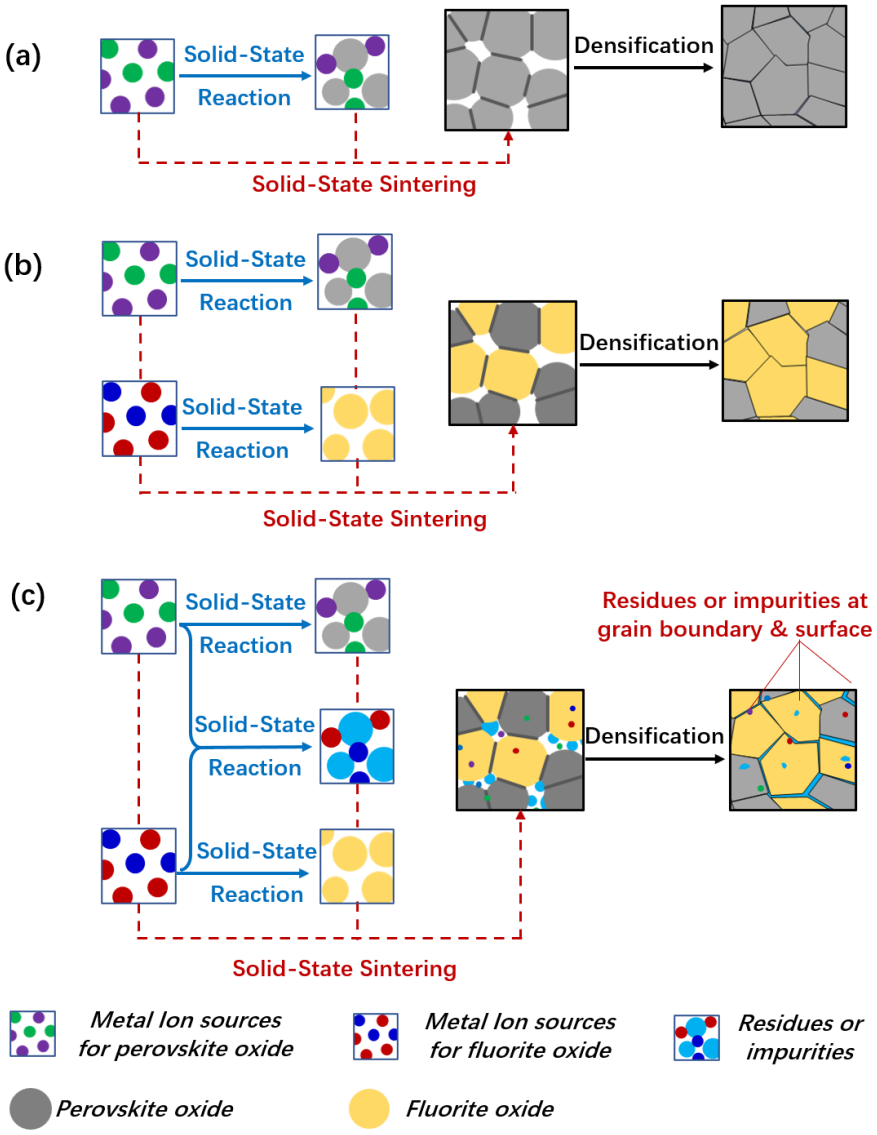

Figure 1. Schematic of the one-step thermal processing (OSTP). (a) single-phase (perovskite) membrane fabrication; dual-phase (perovskite-fluorite) membrane in the case of **(b)** matched and **(c)** mismatched reaction and ramping rates.

In addition to the more complex sintering kinetics of dual-phase membranes via OSTP, this study also focuses on the feasibility of advancing the OSTP approach to preparing four-channel hollow fiber membranes. The sintering kinetics (mainly the ramping rate) and its impacts on membrane morphology, crystal structure, phase stability and permeation properties have been

systematically investigated, followed by outlining prominent potentials of utilizing the dual-phase four-channel hollow fiber membranes for applications with enriched carbon dioxide, such as catalytic membrane reactor (dry reforming and carbon dioxide dissociation) and oxyful combustion (O_2/CO_2), where sufficient oxygen permeation and chemical stability under carbon dioxide atmosphere are both important.

2. Experimental

2.1. One-step thermal processing of dual-phase hollow fiber.

The 60wt.%$Ce_{0.8}Sm_{0.2}O_{2-\delta}$-40wt.%$SrCo_{0.9}Nb_{0.1}O_{3-\delta}$ dual-phase membrane was fabricated via the OSTP approach. Stoichiometric amounts of raw materials $SrCO_3$, Co_2O_3, Nb_2O_5, CeO_2 and Sm_2O_3 (analytical grade) were mixed with polyetherimide (PEI) and 1-methyl-2-pyrrolidone (NMP) via ball milling for 24 h. The spinning suspension obtained consisted of 66 wt.% solids, 27 wt.% NMP and 7 wt.% PEI. Deionized water was used as both internal and external coagulants. The four-channel hollow fiber precursors were obtained by extruding the spinning suspension through a spinneret, the details of which have been described elsewhere [20]. Injection rate of the internal coagulant was 8 mL min^{-1}, while the one for suspension was kept at 3 mL min^{-1}. After the phase inversion process, hollow fiber precursors were dried at room temperature for 24 h, and before being sintered at 1563 K for 10 h in static air, with the heating and cooling rates ranging from 2 K min^{-1} to 5 K min^{-1}, to obtain gas-tight SDC-SCN four-channel hollow fibers. For reference, we also prepared SDC-SCN four-channel hollow fibers via traditional two-step thermal processing approach (TSTP, including separate steps of oxides calcination and membrane sintering) where pre-prepared SDC and SCN oxide powders were used for preparing the spinning suspension.

2.2. Synthesis of SDC and SCN powders

To investigate phase structure and adsorption property of single-phase oxides, we synthesized single-phase SDC and SCN powders using traditional methods. SDC powder was synthesized by an EDTA-citric acid complex sol-gel method. The required amounts of $Sm(NO_3)_3$ and $Ce(NO_3)_3$ (analytical grade) were dissolved in an aqueous solution. EDTA and citric acid were dissolved in deionized water, and the pH of the solution was adjusted to approximately 7 by the addition of aqueous ammonia. The nitrate solution was added dropwise to the EDTA-citric acid complex solution, with the molar ratio of metal ion: citric acid: EDTA: at 1:1:2. A gel was obtained by evaporating water at 338 K under stirring, followed by pre-fire in air at 473 K to remove organic compounds, and calcination at 1073 K for 5 h under a static air atmosphere to obtain SDC powder. SCN powder was prepared by a solid-state method. The stoichiometric amounts of $SrCO_3$, Co_2O_3 and Nb_2O_5 were mixed in ethanol, and ball-milled for 24 h. After evaporating ethanol, the mixture was calcined at 1373 K for 5 h under a static air atmosphere to obtain SCN powder.

2.3. Characterizations

The morphologies of hollow fiber samples were investigated using a scanning electron microscope (SEM, Hitachi S-4800, Japan) equipped with a backscattered electron (BSE) detector. A focused ion beam (FIB, FEI, Helios Nanolab 600i, United States) was employed to extract a cross-section lamella (90 nm thickness, **Fig. 2**) from the SDC-SCN grain boundary interface. The FIB workstation was operated at a voltage of 15 kV. The sites of interest were protected from the gallium

ion beam by locally depositing a carbon layer followed by the application of a thicker platinum layer. The gallium ion beam was then used to carve out a lamella which was mounted on a transmission electron microscopy (TEM) grid and ion milled until it became electron-transparent. The as-prepared lamella was observed using high-resolution transmission electron microscopy (HRTEM, FEI, Tecnai G2 F30 S-TWIN, America) operated at an accelerating voltage of 300 kV and equipped with an energy dispersive X-ray spectrometer (EDX).

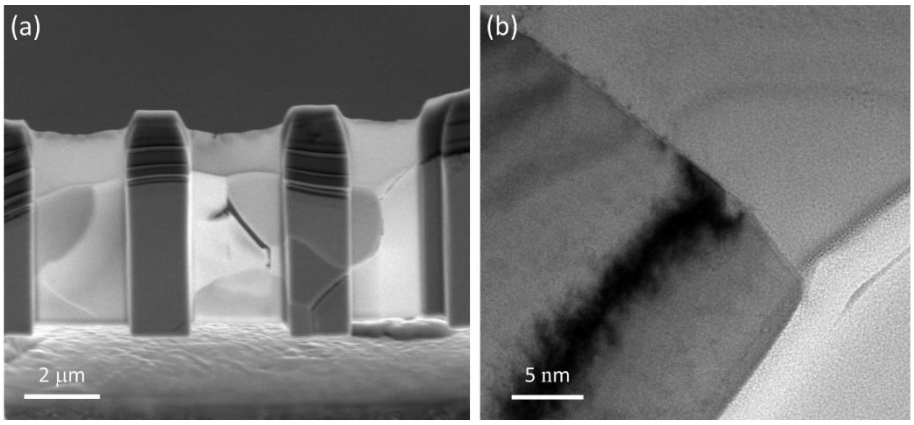

Figure 2. Cross-section of lamella at the SDC-SCN grain boundary extracted by the FIB technique. (a) Overview and **(b)** Close view.

Phase structures of the samples were characterized by X-ray diffraction (XRD, Bruker, model D8 advance, Germany) in the range of $20° \leq 2\theta \leq 80°$ and at a step width of 0.02°. The variation of crystal structures of the dual-phase membrane (sintered at 2K min^{-1} and 1563 K for 10 h) at high temperature was characterized by an in-situ XRD instrument equipped with a high-temperature attachment (in-situ HTXRD, Philips, X'Pert Pro). The samples were tested in air from 298 K to 1273 K with a heating rate of 2 K min^{-1} and each temperature point was maintained for 30 min to achieve thermal equilibrium before diffraction data collection. All diffraction patterns were collected by step scanning at increments of 0.05° in the range $20° \leq 2\theta \leq 80°$. The mechanical strength of the dual-phase hollow fiber membrane was measured by a three-point bending test performed using a tensile tester (Model CMT6203, USA) with a load cell of 5kN.

Carbon dioxide adsorption/desorption (CO_2-TPD) experiments were performed using high-temperature chemisorption instrument (MicrotractBEL, BELCAT II, Japan). Powder specimens (150 mg) were placed in a U-shaped quartz tube and preheated in flowing pure carbon dioxide (20 mL min 1) to 973 K, held for 2 h, cooled to room temperature, and re-heated to 1173K at a rate of 10 K min^{-1}. The effluent gases were monitored using a mass spectrometer (Hiden Analytical, QIC-20, United Kingdom).

2.4. Oxygen permeation

The setup used to carry out the oxygen permeation experiments in the hollow fiber membrane is describe in detail elsewhere [21]. The supply of various gases was controlled by mass flow controllers (Sevenstar, CS200, China). The air flow rate at the feed side (shell side) was 120 mL min^{-1}, and helium flow rate at the sweep side (lumen side) was 60 mL min^{-1}. The temperature around the samples was controlled by a high-temperature tubular furnace (HF-Kejing, OTF-1200X, China). The gas composition at the sweep side outlet was determined using an online gas chromatographer (Agilent, 7820A, Germany) equipped with a 5A molecular sieve column. Unlike tubular membranes and disk-like membranes, the membrane area of multi-channel hollow fiber membrane for oxygen permeation flux calculation is difficult to obtain. To be consistent with the literatures [17, 22], the outermost surface area of the multi-channel hollow fiber membrane was used for calculation in this study. The possible oxygen leakage due to imperfect sealing at high temperatures was monitored through the mole fraction of nitrogen (79 mol. % in the feed side) that leaked into the sweep side. The experiments were conducted only if the nitrogen leakage was below 0.5 mol.%.

2.5. Carbon dioxide stability

Experiments on the stability and reversibility of the membrane exposed to carbon dioxide were performed in the setup for oxygen permeation described in the Section 2.4. Air (120 mL·min-1) was fed into the feed side (shell side), while carbon dioxide and helium (60 mL·min-1) were alternatively fed into the sweep side (lumen side). The membrane was exposed to 100% carbon dioxide for 24, 24, 24, 24 and 100 h. After each exposure, the sweep side was switched to helium for 4 h to examine the recovery of oxygen flux.

3. Results and discussion

3.1. Morphology and phase structure

Microstructure of the dual-phase four-channel hollow fiber membrane prepared via the OSTP approach was examined by SEM. As shown in **Fig. 3a**, the membrane forms an asymmetrical four-channel structure. The outermost diameter of the hollow fiber is 3.05 ±0.05 mm. The shape of the inner channel is close to an ellipse. Graphical measurements were used to obtain the circumference of the elliptical channels. The circumferences of the outermost hollow fiber and sum of the four inner channels (based on **Fig. 3a)** are 9.6 ±0.3 mm and 9.8±0.2mm, respectively. This indicates that surface areas of the outermost surface and the inner surface are similar. Large amounts of closely packed finger-like pores are distributed in the bulk of hollow fiber skeleton while sponge-like pores are located near external and internal surfaces and sandwiched between layers of finger-like pores (**Fig. 3b**). It has been demonstrated that both the finger-like and sponge-like layers greatly affect membrane properties such as mechanical strength and oxygen permeation. The finger-like pores have very low tortuosity, which are beneficial in terms of reducing mass transfer resistance and thus

increasing oxygen permeation [23, 24]. After high-temperature sintering, the sponge-like layers become gas tight, and provides the majority of mechanical strength and perm-selectivity to oxygen [25]. From the view of top surface (**Fig. 3c**), there is a dense surface with grains distributed homogenously. The insert in **Fig. 3c** presents a micrograph of the top membrane surface using BSE imaging. It shows a distinct contrast image when the light area is SDC and the dark area is SCN, indicating a uniform distribution of grain particles of the two oxides. Room-temperature XRD further confirms the formation of the two oxides via the OSTP approach. Shape and clear characteristic peaks of SDC and SCN identified in the dual-phase membrane (**Fig. 3d**) match well with diffraction peaks of the reference samples made of single-phase fluorite and perovskite oxides (the major diffraction angles for single phase SDC and SCN are 28.5^{o}, 33.0^{o}, 47.3^{o} and 56.1^{o}, and 32.5^{o}, 40.1^{o}, 46.8^{o} and 58.2^{o}, respectively). As shown in **Fig. 3 c&d**, some small particles are found on the membrane surface, but not detected by XRD. This may be due to the detection limit of XRD, and the high-crystallinity masks from the SDC and SCN. Formation of impurity particles on the membrane surface will be discussed in detail later.

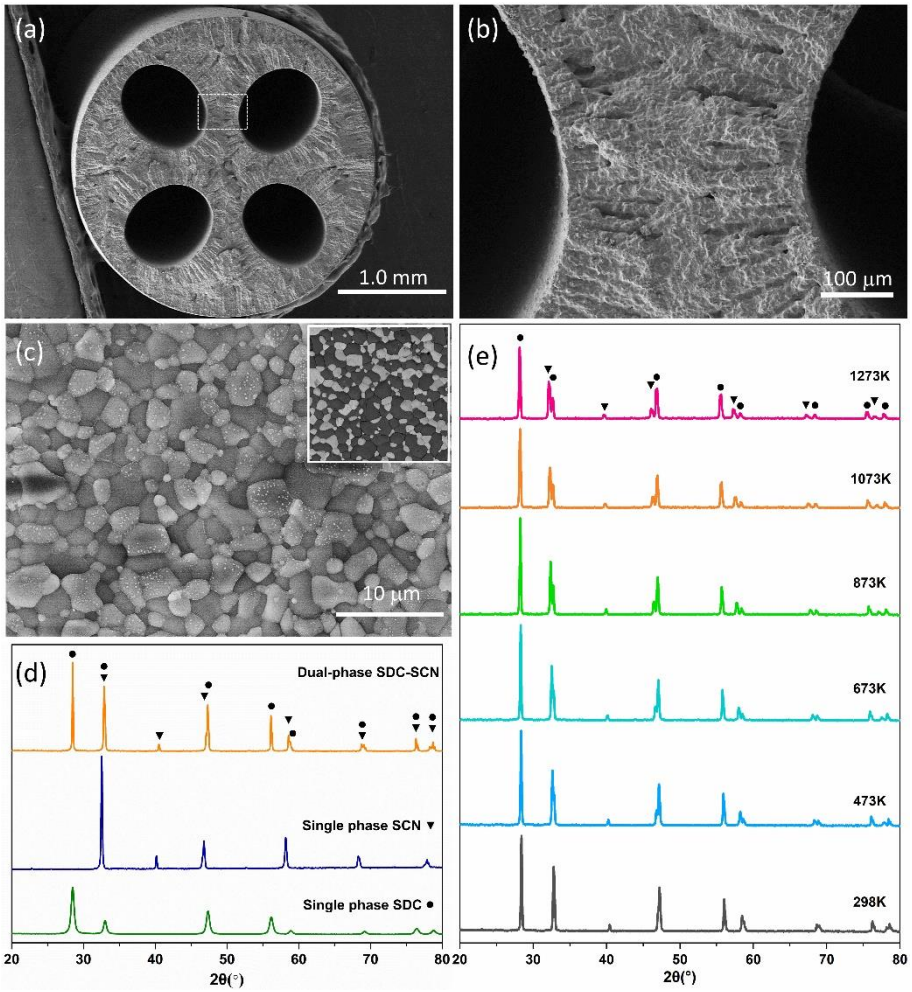

Figure 3. **Microstructure and phase structure of the dual-phase hollow fiber membrane fabricated via the OSTP approach (2K min^{-1} ramping rate, 1563 K for 10 h).** SEM micrographs: **(a)** cross-section overview; **(b)** in the region of the skeleton marked on **a**; **(c)** top-view of hollow fiber outermost surface, insert is the BSE micrograph. **(d)** XRD patterns of dual-phase SDC-SCN membrane (OSTP) and reference samples of single phase SDC (sol-gel method) and SCN (solid-state method). **(e)** *in-situ* high-temperature XRD patterns of dual-phase SCF-SCN membrane (OSTP approach).

Effects of temperature on the chemical compatibility between perovskite and fluorite was also studied via in-situ XRD, between temperatures of 298–1273 K and at a temperature step of 200 K. As shown in **Fig. 3e**, diffraction peaks of both the SCN perovskite phase and SDC fluorite phase are sharp and clear, with no additional phases observed during the process of heating. Note that the diffraction peaks shift to a low angle at elevated temperatures owing to thermal expansion of oxide lattice [26]. Meanwhile, diffraction peaks of the two phases are partially overlapped at room

temperature; however, the difference in thermal expansion rates at elevated temperatures leads to the separation of diffraction peaks. For example, for temperatures higher than 473 K, a split of the two-phase diffraction peaks can be observed; while at 1273 K, the overlapped peaks have been separated completely. These results indicate a good compatibility of bulk SDC and SCN at elevated temperatures.

To further understand and characterize structural changes occurring at the grain boundary of the two oxides after OSTP, we extracted electron-transparent lamellae around the interface and examined them by TEM and EDX. **Fig. 4a** shows straight and smooth grain boundaries and two bulk phases (marked as I and II). HRTEM was employed to analyze the crystal evolution of materials at an atomic scale. The oxides exhibit a high crystallinity. Within each grain, continuous single-directional lattice fringes can be observed on the bulk of the left and right half sides. The marked d-spacing of 0.313 nm corresponds to the interplanar distance of the SDC [1 1 1] lattice planes, which agrees to the diffraction data of SDC (ICDD NO. is 75-0158). The marked d-spacing of 0.375 nm corresponds to the interplanar distance of the SCN [1 0 0] lattice planes [27]. The corresponding EDX was obtained around the grain boundary. Ce and Sm are mainly concentrated in area ***I***, while elements of Sr and Co are mainly concentrated in area ***II***, indicating that area ***I*** is the SDC phase and area ***II*** is the SCN phase. To explore cation exchanges (or solid-state reaction) between the two oxides at the grain boundary interface, elemental compositions (expressed as an atomic fraction) at various points of interest marked with numbers (in **Fig. 4a**) are plotted in **Fig. 4b**. These data indicate that the bulk of the perovskite and the fluorite in the vicinity of the grain boundary interface display similar compositions, equivalent to the composition of nominal perovskite and fluorite and as thus unaffected by the OSTP approach. In contrast, the grain boundary

interface region at a width of approximately 20-30 nm experience drastic changes in composition. Sr/Co and Sm/Ce ions are found enriched on the side of SDC and SCN, respectively. Ion exchange is inevitable at the interface during high-temperature processing. However, it can be restricted to the nanometer level and the related effect on oxygen permeation can be controlled within a small range.

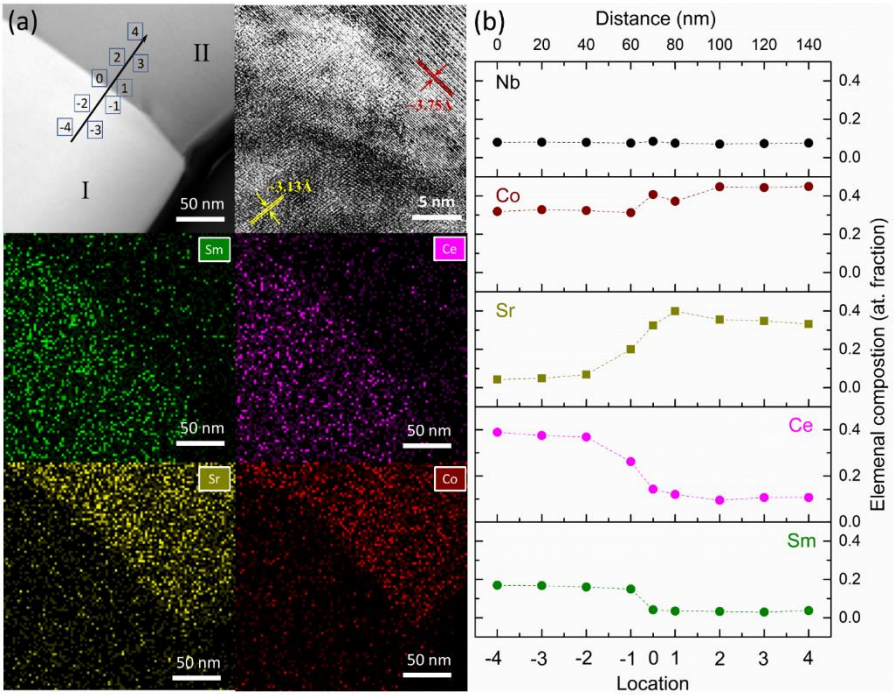

Figure 4. Cation exchange between perovskite oxide and fluorite oxide at the grain boundary of the dual-phase hollow fiber membrane fabricated via OSTP approach (2K min^{-1} ramping rate, 1563 K for 10 h) (a) TEM and HRTEM micrographs around the SDC and SCN grain boundary with corresponding elemental maps obtained by EDX analysis. **(b)** Elemental composition (normalized to 1) at different point locations marked on the micrograph shown in **a.**

3.2. Sintering kinetics

In the OSTP approach, solid-state reactions of raw chemicals and solid-state sintering of membrane occurred simultaneously at elevated temperatures, which can thus be considered as an in-situ reactive sintering process. As discussed in Introduction, the scenario is even more complex for a heterogeneous system containing more than one phase; therefore, it is important to study the

reactive sintering kinetics and its effects on microstructure and phase structure of the dual-phase hollow fiber membrane. It has been widely accepted that ramping rate is one of the most important factors determining the rates of reaction and densification [28]. Therefore, in this study, sintering kinetics were investigated by means of a stepwise ramping rate accompanied by SEM and oxygen permeation flux.

The surface morphologies of the dual-phase hollow fiber at ramping rates of 2, 3, 4, and 5 K min^{-1} are shown in **Fig. 5a**. The figure clearly shows a dense surface with homogenously distributed perovskite and fluorite oxide grains. As the SEM was operated at a high accelerating voltage, the electron microscope micrographs provide a light/dark contrast between perovskite SCN (dark-colored grains) and fluorite SDC phases (light-colored grains). A large number of brighter nanoparticles are found on the surface of the SDC grains and at grain boundaries at the ramping rates of 2 and 3 K min^{-1}. Notably, these brighter nanoparticles on the SDC surfaces concentrate at the grain boundary when the ramping rate increases to 4 K min^{-1}, while impurities are barely observed at a higher ramping rate of 5 K min^{-1}. Since the nanoparticles are too small to be detected by XRD, TEM and EDX analyses were used to identify the nanoparticles. As shown in **Fig. 5b**, irregular particles with the size of 200-300 nm are found on the SDC bulk surface. From EDX, the nanoparticles are identified as cobalt oxide (CoO_x, the stoichiometric coefficient *x* could not be precisely confirmed by EDX). The formation of impurities is closely related to the formation enthalpy of SDC and SCN, but these have rarely been reported in literature. Lu et al. [29] provided a simple method to estimate the enthalpy of formation of complex oxides with an error of less than 1%. Based on this method, the estimated enthalpies of formation of $Ce_{0.8}Sm_{0.2}O_2$ and $SrCo_{0.9}Nb_{0.1}O_3$ are calculated as -1053.3 and -954.3 kJ/mol (298.15 K), respectively. For the convenience of

calculation, the nonstoichiometric coefficient δ is set to zero. Thermodynamically, lower ramping rates (lower temperature) favor the formation of the two oxides. However, kinetically, the chemical reaction occurred by solid-state diffusion of ions, which is characterized by a slow kinetic rate. The reaction starts at the points of contact between the initial solid components and continues by ionic interdiffusion through the product phase. In this case, the degree of mixing and concentration of raw chemicals are key factors for a faster reaction [30]. A high concentration of the binary metal oxide $Ce_{0.8}Sm_{0.2}O_{2-\delta}$ (60 wt.%) is more active in the subsequent heat-treatment steps than the ternary metal oxide $SrCo_{0.9}Nb_{0.1}O_{3-\delta}$ (60 wt.%). This evidence might support an assumption that a lower ramping rate favors of the formation of SDC, while a high ramping rate favors the formation of SCN. The initially generated SDC particles physically block the SCN formation and result in isolated reactants (such as cobalt oxide) on the SDC and at grain boundaries, as illustrated in **Fig. 1c**. For reference, we also prepared SDC-SCN four-channel hollow fibers via traditional TSTP approach where SDC and SCN oxide powders were used in the spinning suspension. The membrane was sintered at a ramping rate of 2 K min^{-1}. As shown in **Fig. 5c**, a clear surface can be observed, indicating that the simultaneous solid-state reaction and sintering in the OSTP approach is the main reason for the formation of nanoparticle impurities.

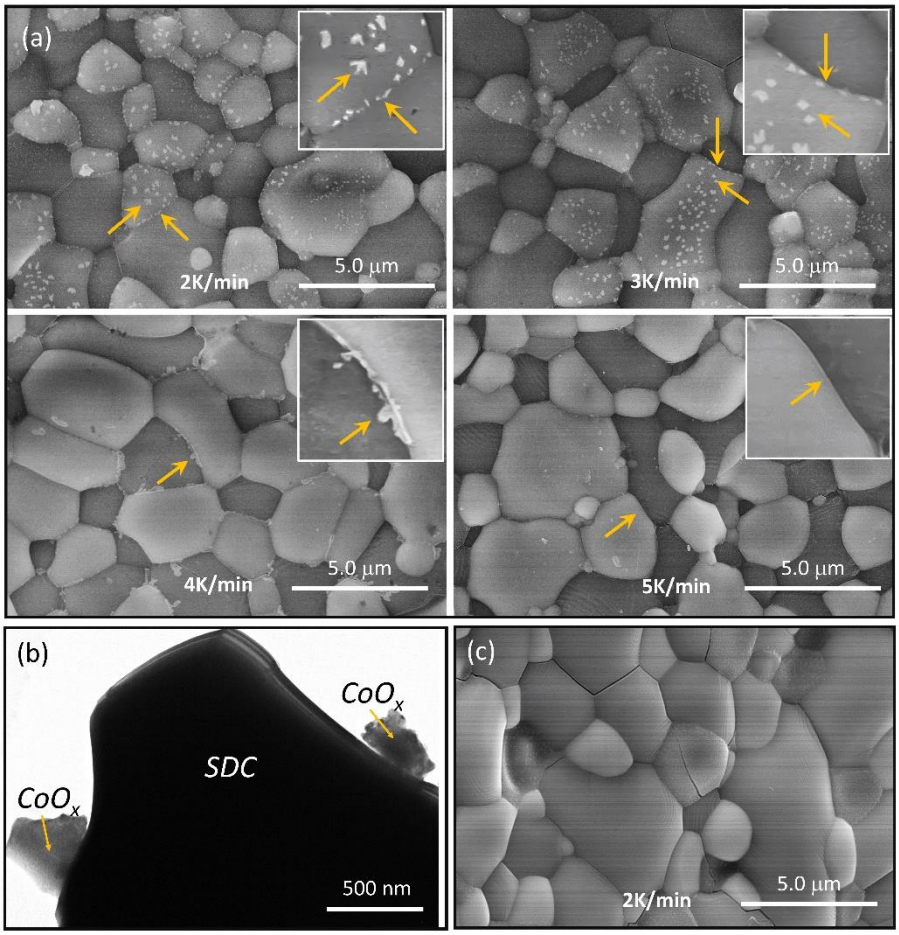

Figure 5. Sintering kinetics on the morphology and permeation flux of the membrane fabricated via the OSTP approach (sintered at 1563 K for 10 h). (a) SEM micrographs of the dual-phase membrane sintered at different rates. Inserts are the magnifications around the grain boundary labeled with arrows; **(b)** TEM micrograph shows the CoOx nanoparticles on SDC; **(c)** SEM micrograph of membrane sintered via TSTP approach where SDC and SCN oxides mixture were used for the spinning solution ;

Ramping rates also have a significant effect on grain size. It can be seen from **Fig. 5a** that grain size of the two oxides increases with the increase in ramping rate. This effect is more obvious to the SCN phase, which is consistent with the analysis of the effects of the ramping rate on oxide formation. Noting that the effects of ramping rate on the phase structure and microstructure of the membrane also directly affect its mechanical strength. The breaking loads of the membrane sintered at 2, 3, 4, and 5 K min^{-1} are 7.61, 7.57, 6.07, and 6.01 N, respectively. The breaking load of the

dual-phase hollow fiber membrane decreases with the increase in the ramping rate, which may be due to the increase in the grain size [30]. However, this effect of ramping rate on membrane strength is unremarkable.

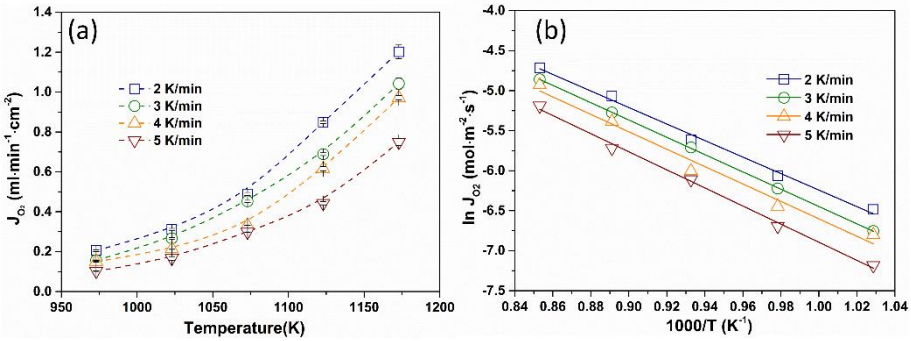

Figure 6 Sintering kinetics on the permeation flux of the membrane fabricated via the OSTP approach (sintered at 1563 K for 10 h). (a) temperature dependence of oxygen permeation flux, and **(b)** Arrhenius plots of oxygen permeation of membrane sintered at different ramping rates.

The oxygen permeation flux was evaluated using the dual-phase four-channel hollow fiber membranes sintered at different ramping rates. As shown in **Fig. 6a**, the membranes sintered at different rates follow a comment trend in which the increase in temperature gradually increases the oxygen permeation flux. This is attributed to the enhanced oxygen surface exchange and bulk diffusion at elevated temperatures. It was observed that a higher ramping rate has a negative effect on membrane permeation flux. For example, at 1173 K, the permeation flux of the membrane sintered at 2, 3, 4, and 5 K min^{-1} are 1.20, 1.04, 0.97 and 0.75 $mL \cdot cm^{-2} \cdot min^{-1}$, receptivity. They show certain competitiveness with fluorite-perovskite based dual-phase hollow fiber membranes reported in literature (Listed in **Table 1**). In our previous study, we found that the oxygen permeation process of SDC-SCN dual-phase membrane is controlled mainly by the surface exchange reactions when the membrane thickness is sufficient thin (thinner than 0.5 mm) [16]. Additionally, the

conductivity of SDC is 1-2 orders of magnitude lower than SCN phase and hence the oxygen permeation is limited mainly by the ionic conductivity from the fluorite phase [10]. In this case, the surface conditions of the SDC grains and three-phase boundaries (TPB, gas-solid boundary at the dual-phase grain boundary) play an important role in surface exchange kinetics and oxygen permeation of the SDC-SCN hollow fiber membrane. Meanwhile, it has been reported that large TPB and cobalt oxide can significantly promote reduction and evolution of oxygen and transfer of oxygen molecular/oxygen intermediates at membrane surface, and improves the oxygen permeation [31-35]. Therefore, a relationship between oxygen permeation and membrane surface morphologies can be established. A lower ramping rate results in a large number of cobalt oxide nanoparticles on the surface of SDC grains and larger TPB, and thus a higher oxygen permeation flux. In addition, the contribution of surface exchanges at the outmost surfaces on the oxygen permeation flux can be observed from the apparent activation energies. From **Fig. 6 b**. the apparent activation energies of the membrane sintered at 2, 3, 4, and 5 K min^{-1} are 85.8±3.9, 90.0±0.5, 90.5±7.1 and 94.0±3.2 kJ mol^{-1}, receptivity. The decoration of cobalt oxide decreases activation energies, due to an increased rate of surface oxygen exchange [35]. In this study, low ramping rates resulted in small grain size, increased grain boundaries (TPB), and a cobalt oxide "impurity" which jointly contribute to increase surface oxygen exchange and oxygen permeation.

Table 1. Oxygen permeation flux through fluorite-perovskite based dual-phase hollow fiber membranes.

Membrane compositions	Geometry	Temp.	Flow rate of sweep gas* $mL \cdot min^{-1}$ (Sweep gas)	Oxygen flux $mL \cdot min^{-1} \cdot cm^{-2}$	Ref.
$Bi_{1.5}Y_{0.3}Sm_{0.2}O_3$-$La_{0.8}Sr_{0.2}MnO_{3-\delta}$	Single-channel hollow fiber	1123K	100 (Helium)	0.52	36
$Zr_{0.84}Y_{0.16}O_{1.92}$-$La_{0.8}Sr_{0.2}MnO_{3-\delta}$	Single-channel hollow fiber	1223K	30 (Helium)	0.282	37
$Zr_{0.84}Y_{0.16}O_{1.92}$-$La_{0.8}Sr_{0.2}Cr_{0.5}Fe_{0.5}O_{3-\delta}$	Single-channel hollow fiber	1223K	30 (Helium)	0.16	38

$Ce_{0.8}Sm_{0.2}O_{1.9}$-$La_{0.8}Sr_{0.2}Cr_{0.5}Fe_{0.5}O_{3-\delta}$	Single-channel hollow fiber	1223K	30 (Helium)	0.50	39
$Ce_{0.8}Sm_{0.2}O_{2-\delta}$-$La_{0.7}Ca_{0.3}CrO_{3-\delta}$	Single-channel hollow fiber	1223K	30 (Helium)	0.31	40
$Ce_{0.8}Sm_{0.2}O_{2-\delta}$-$La_{0.8}Sr_{0.2}MnO_{3-\delta}$	Single-channel hollow fiber	1223K	30 (Helium)	0.43	41
$Ce_{0.85}Sm_{0.15}O_{1.925}$-$Sm_{0.6}Sr_{0.4}Al_{0.3}Fe_{0.7}O_{3-\delta}$	Single-channel hollow fiber	1223K	100 (Helium)	1.026	42
$Pr_{0.1}Gd_{0.1}Ce_{0.8}O_{2-\delta}$-$CoFe_2O_4$†	Single-channel hollow fiber	1273K	150 (Helium)	0.54	8
$Ce_{0.9}Gd_{0.1}O_{2-\delta}$-$La_2NiO_{4+\delta}$‡	Single-channel hollow fiber	1223K	100 (Helium)	1.47	43
$Ce_{0.8}Sm_{0.2}O_{2-\delta}$-$SrCo_{0.9}Nb_{0.1}O_{3-\delta}$	Four-channel hollow fiber	1173K	60 (Helium)	1.20	This work

* Feed gas is atmospheric air
† Spinel structure
‡ Ruddlesden-Popper type perovskite structure

3.3 Carbon dioxide adsorption/desorption

Carbon dioxide is present in many membrane processes, such as catalytic membrane reactors, oxyfuel combustion, and other carbon dioxide separation and capture processes. Interactions between membrane materials (mostly perovskite oxides) and carbon dioxide are inevitable, no matter reversible or irreversible, and impairs oxygen permeation and even membrane stability. Oxygen permeation of the dual-phase hollow fiber membrane was investigated using different concentrations of carbon dioxide at the sweep side (air was at the feed side). Notably, it has been reported that the present of carbon dioxide at the feed side (air side) decreases the oxygen permeation, however the impact of carbon dioxide on the oxygen permeation is inferior to that applied at the sweep side [44]. Therefore, mainly the effects of carbon dioxide at the sweep were discussed. The concentration of carbon dioxide at the sweep side ranged from 0% to 100 % with a stepwise concentration of 20 %. As shown in **Fig.7a**, in the presence of carbon dioxide, the oxygen

permeation flux decreases with an increase in the carbon dioxide concentration at the sweep side. In particular, for a sweep with 100% carbon dioxide, the oxygen permeation flux is almost zero. Such a sudden cessation of oxygen flux has been widely reported for perovskite membranes and is considered mainly due to the interaction of carbon dioxide and membrane materials [44, 45]. Lin et al. [46] systematically studied the behavior of carbon dioxide adsorption and reaction on perovskite oxides. The carbon dioxide adsorption process for dense particles can be illustrated by the shrinking-core model, where carbonation reactions of carbon dioxide with membrane materials occurred at the surface of the dense perovskite oxide and produced a porous product layer on the unreacted perovskite core. Both carbon dioxide and oxygen can transport out of or into the porous carbonate layers. The solid carbonates (which are non-oxygen-permeable) on the membrane surface have the negative effect of blocking active sites for oxygen permeation. The blockage is further strengthened with more concentrated carbon dioxide (more coverage by carbonates on the membrane surface). The blockage of oxygen permeation from carbon dioxide can be revealed by studying the expansion behavior of the membrane at elevated temperatures, as the lattice expansion is associated with the oxygen exchange between the gas and solid. As shown in **Fig. 7b**, the expansion curve obtained in carbon dioxide linearly increases with the temperature, which is attributed to the atomic vibrations of the lattice during the heating process. However, deviations of the linear change (i.e., slope changes at 600-800 (I), 800-1000 (II) and >1000 K (III)) were observed in the membrane expansion curve obtained in air. This is mainly caused by the loss of a large amount of lattice oxygen, commonly known as chemical expansion [26]. Obviously, the carbon dioxide adsorbed on the membrane surfaces hinders oxygen transfer from the solid to gas phase.

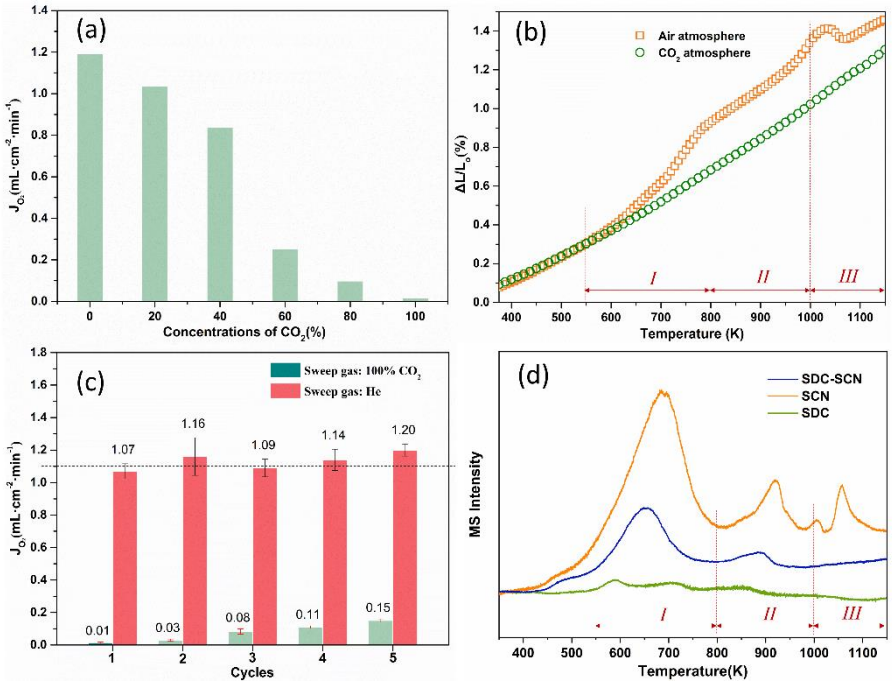

Figure 7. Effect of carbon dioxide on the dual-phase hollow fiber membrane fabricated via the OSTP approach (2K min^{-1} ramping rate, 1563 K for 10 h). **(a)** Oxygen permeation flux at 1173 K with different concentrations of carbon dioxide at the sweep side; **(b)** high-temperature expansion in air and pure carbon dioxide atmosphere; **(c)** reversibility of the oxygen permeation fluxes at 1173 K as a function of time while periodically changing the sweep gases. (in Cycle 1-5 the sweep side of membrane was exposed to flowing carbon dioxide for 24, 24, 24, 24, and 100 h, respectively); **(d)** CO_2-TPD profiles of SCN, SDC, and SDC-SCN powder samples.

The ability of recovering from carbon dioxide exposure and carbon dioxide tolerance were further investigated by periodically exposing the sweep side of the membrane to carbon dioxide and helium. The membrane was exposed to 100% carbon dioxide for 24, 24, 24, 24, and 100 h. After each exposure, the sweep side was switched to helium for 4 h to examine the recovery of oxygen permeation. As shown in **Fig. 7c**, the membrane has a low oxygen flux when it was exposed to 100% carbon dioxide, confirming the blockage of oxygen permeation by carbon dioxide. When carbon dioxide was removed from the sweep side, the membrane displays an immediate oxygen recovery and the recovered oxygen flux fluctuates to approximately 1.13 mL cm^{-2} min^{-1}, and is very close to

the original value of 1.20 mL cm^{-2} min^{-1}. The membrane in each of the first four cycles (***Cycle 1-4***) was exposed to carbon dioxide for 24 h and then further extended to 100 h in ***Cycle 5***. The dual-phase membrane shows good carbon dioxide tolerance and flux resilience, and the oxygen flux can be restored to 1.2 mL cm^{-2} min^{-1}. The resilience from carbon dioxide exposure indicates that carbon dioxide adsorption and carbonation are reversible. To confirm this, CO_2-TPD experiments were performed on a dual-phase membrane (single-phase SDC and SCF were used as reference). As shown in **Fig. 7d**, perovskite oxide and fluorite oxide exhibit different carbon dioxide adsorption/desorption behavior. Desorption peaks appear at approximately 600-800 (***I***), 800-1000 (***II***) and >1000 K (***III***) for the SCN oxide samples. This phenomenon is consistent with the membrane expansion behavior in carbon dioxide shown in **Fig. 6b**. These results indicate a strong interaction between carbon dioxide and metal oxides. Peaks were derived from the chemisorption of carbon dioxide on the SDC surface [48] and the decomposition of metal carbonates or metal oxides (e.g., cobalt carbonate, strontium carbonate or cobalt oxide)[48-50].Very weakly eluted carbon dioxide was detected in the SDC sample, indicating an inert feature of SDC to carbon dioxide. Therefore, the existence of SDC in the dual-phase membrane can effectively reduce the adsorption and carbonation reactions, which result in carbon dioxide desorption peaks with lower intensity. Note that the temperatures of carbon dioxide desorption and carbonate decompositions are lower than the membrane operation temperature (1173 K), demonstrating the recovery capability of the membrane (in **Fig. 7c**) at the current operating temperature.

4. Conclusions

$Ce_{0.8}Sm_{0.2}O_{2-\delta}$–$SrCo_{0.9}Nb_{0.1}O_{3-\delta}$ (SDC-SCN) dual-phase four-channel hollow fiber membranes were successfully fabricated via a one-step thermal process (OSTP) by directly using metal oxides and carbonates as metal ion sources and with only one high-temperature sintering throughout membrane fabrication. The as-prepared four-channel hollow fiber shows a typical asymmetric structure and dense surface with homogenously distributed perovskite and fluorite oxide grains. Ion exchange was observed at the SDC/SCN grain boundaries after OSTP, which can be limited to the nanometer level (less than 30 nm). It was demonstrated that the membrane morphology, phase structure and permeation properties are closely related to the ramping rate in OSTP, which affects both the solid-state reaction and solid-state sintering. A low ramping rate (2K min^{-1}) results in a dual-phase hollow fiber membrane with a smaller grain size, increased grain boundaries, and decoration by cobalt oxide nanoparticles, and with a higher oxygen permeation rate of 1.20 $mL \cdot cm^{-2} \cdot min^{-1}$ at 1173 K. The existence of SDC in the dual-phase membrane can effectively suppress the adsorption and carbonation reactions between carbon dioxide and metal oxides. The dual-phase four-channel hollow fiber membrane shows good carbon dioxide tolerance and flux recovery ability after long-term carbon dioxide exposure (more than 100 h), which demonstrates that the oxygen flux can be restored to 1.2 mL cm^{-2} min^{-1}.

Acknowledgements

This work was supported by the Natural Science Foundation of China (21706118,21706117), the Natural Science Foundation of Jiangsu (BK20170978, BK20170970), the State Key Laboratory

of Material-Oriented Chemical Engineering (ZK201609, KL18-10) and the Topnotch Academic Programs Project of Jiangsu Higher Education Institutions (TAPP)

References

[1] C. Zhang, J. Sunarso, S. Liu, Designing CO_2-resistant oxygen-selective mixed ionic-electronic conducting membranes: guidelines, recent advances, and forward directions, *Chemical Society Reviews*, 46 (2017) 2941-3005.

[2] G. Zhang, W. Jin, N. Xu, Design and fabrication of ceramic catalytic membrane reactors for green chemical engineering applications, *Engineering*, 4 (2018) 848-860.

[3] A. Leo, S.M. Liu, J.C.D. da Costa, Development of mixed conducting membranes for clean coal energy delivery, *International Journal of Greenhouse Gas Control*, 3 (2009) 357-367.

[4] Y.Y. Wei, W.S. Yang, J. Caro, H.H. Wang, Dense ceramic oxygen permeable membranes and catalytic membrane reactors, *Chemical Engineering Journal*, 220 (2013) 185-203.

[5] Y. Alqaheem, A. Thursfield, G. Zhang, I.S. Metcalfe, The impact of sulfur contamination on the performance of $La_{0.6}Sr_{0.4}Co_{0.2}Fe_{0.8}O_{3-\delta}$ oxygen transport membranes, *Solid State Ionics*, 262 (2014) 262-265.

[6] K. Mezghani, A. Hamza, Application of $Ba_{0.5}Sr_{0.5}Co_{0.8}Fe_{0.2}O_{3-\delta}$ membranes in an oxy-fuel combustion reactor, *Journal of Membrane Science*, 518 (2016) 254-262.

[7] G.H. He, Z.W. Cao, W.Y. Liang, Y. Zhang, X. Liu, J. Caro, H.Q. Jiang, Codoping strategy to improve stability and permeability of $Ba_{0.6}Sr_{0.4}FeO_{3-\delta}$-based perovskite membranes, *Industrial & Engineering Chemistry Research*, 55 (2016) 10386-10393.

[8] X. Bi, X. Meng, P. Liu, N. Yang, Z. Zhu, R. Ran, S. Liu, A novel CO_2-resistant ceramic dual-phase hollow fiber membrane for oxygen separation, *Journal of Membrane Science*, 522 (2017) 91-99.

[9] H. Cheng, X. Wang, X. Meng, B. Meng, J. Sunarso, X. Tan, L. Liu, S. Liu, Dual-layer $BaCe_{0.8}Y_{0.2}O_{3-\delta}$-$Ce_{0.8}Y_{0.2}O_{2-\delta}$/$BaCe_{0.8}Y_{0.2}O_{3-\delta}$-Ni hollow fiber membranes for H_2 separation, *Journal of Membrane Science*, 601 (2020).

[10] C. Li, W.P. Li, J.J. Chew, S.M. Liu, X.F. Zhu, J. Sunarso, Rate determining step in SDC-SSAF dual-phase oxygen permeation membrane, *Journal of Membrane Science*, 594 (2020) 2.

[11] X.F. Zhu, Q.M. Li, Y.F. He, Y. Cong, W.S. Yang, Oxygen permeation and partial oxidation of

methane in dual-phase membrane reactors, *Journal of Membrane Science*, 360 (2010) 454-460.

[12] X. Zhu, Q. Li, Y. Cong, W. Yang, Syngas generation in a membrane reactor with a highly stable ceramic composite membrane, *Catalysis Communications*, 10 (2008) 309-312.

[13] L.L. Cai, S.Q. Hu, Z.W. Cao, H.B. Li, X.F. Zhu, W.S. Yang, Dual-phase membrane reactor for hydrogen separation with high tolerance to CO_2 and H_2S impurities, *AIChE Journal,* 65 (2019) 1088-1096.

[14] W.P. Li, Z.W. Cao, L.L. Cai, L.X. Zhang, X.F. Zhu, W.S. Yang, H_2S-tolerant oxygen-permeable ceramic membranes for hydrogen separation with a performance comparable to those of palladium-based membranes, *Energy Environmental Science*, 10 (2017) 101-106.

[15] L. Cai, S. Hu, Z. Cao, H. Li, X. Zhu, W. Yang, Dual-phase membrane reactor for hydrogen separation with high tolerance to CO2 and H2S impurities, *AIChE Journal*, 65 (2019) 1088-1096.

[16] S. Guo, Z. Liu, J. Zhu, X. Jiang, Z. Song, W. Jin, Highly oxygen-permeable and CO_2-stable $Ce_{0.8}Sm_{0.2}O_{2-\delta}$-$SrCo_{0.9}Nb_{0.1}O_{3-\delta}$ dual-phase membrane for oxygen separation, *Fuel Processing Technology*, 154 (2016) 19-26.

[17] T. Wang, Z. Liu, X. Xu, J. Zhu, G. Zhang, W. Jin, Insights into the design of nineteen-channel perovskite hollow fiber membrane and its oxygen transport behaviour, *Journal of Membrane Science*, 595 (2020).

[18] J. Zhu, Z. Dong, Z. Liu, K. Zhang, G. Zhang, W. Jin, Multichannel mixed-conducting hollow fiber membranes for oxygen separation, *AIChE Journal*, 60 (2014) 1969-1976.

[19] J. Zhu, T. Wang, Z. Song, Z. Liu, G. Zhang, W. Jin, Enhancing oxygen permeation via multiple types of oxygen transport paths in hepta-bore perovskite hollow fibers, *AIChE Journal*, 63 (2017) 4273-4277.

[20] J. Zhu, G. Zhang, G. Liu, Z. Liu, W. Jin, N. Xu, Perovskite hollow fibers with precisely controlled cation stoichiometry via one-step thermal processing, *Advanced Materials*, 29 (2017).

[21] K.P. Jiang, Z.K. Liu, G.R. Zhang, W.Q. Jin, A novel catalytic membrane reactor with homologous exsolution-based perovskite catalyst, *Journal of Membrane Science*, 608 (2020) 10.

[22] Y.S. Chi, T. Li, B. Wang, Z.T. Wu, K. Li, Morphology, performance and stability of multi-bore

capillary La0.6Sr0.4Co0.2Fe0.8O3-delta oxygen transport membranes, *Journal of Membrane Science*, 529 (2017) 224-233.

[23] T. Li, T. Kamhangdatepon, B. Wang, U.W. Hartley, K. Li, New bio-inspired design for high-performance and highly robust $La_{0.6}Sr_{0.4}Co_{0.2}Fe_{0.8}O_{3-\delta}$ membranes for oxygen permeation, *Journal of Membrane Science*, 578 (2019) 203-208.

[24] A. Leo, S. Liu, J.C.D. da Costa, The enhancement of oxygen flux on $Ba_{0.5}Sr_{0.5}Co_{0.8}Fe_{0.2}O_{3-\delta}$ (BSCF) hollow fibers using silver surface modification, *Journal of Membrane Science*, 340 (2009) 148-153.

[25] B.F.K. Kingsbury, K. Li, A morphological study of ceramic hollow fibre membranes, *Journal of Membrane Science*, 328 (2009) 134-140.

[26] G.R. Zhang, Z.K. Liu, N. Zhu, W. Jiang, X.L. Dong, W.Q. Jin, A novel Nb_2O_5-doped $SrCo_{0.8}Fe_{0.2}O_{3-\delta}$ oxide with high permeability and stability for oxygen separation, *Journal of Membrane Science*, 405 (2012) 300-309.

[27] C.-Y. Yoo, J.H. Park, D.S. Yun, Y.A. Lee, K.S. Yun, J.H. Lee, H. Yoon, J.H. Joo, J.H. Yu, Unraveling crystal structure and transport properties of fast ion conducting $SrCo_{0.9}Nb_{0.1}O_{3-\delta}$, *Journal of Physical Chemistry C*, 120 (2016) 22248-22256.

[28] Y.T. Liu, K. Li, Preparation of $SrCe_{0.95}Yb_{0.05}O_3$-alpha hollow fibre membranes: Study on sintering processes, *Journal of Membrane Science*, 259 (2005) 47-54.

[29] Q. Hongliang, L.I.U. Chang, J.I. Yuanhui, Y.A.O. Wenjun, F. Xin, L.U. Xiaohua, Simple estimation method for thermodynamic data of complex oxysalt minerals, *Journal of Chemical Industry and Engineering*, 61 (2010) 544-550.

[30] M.N. Rahaman, Sintering of Ceramics, CRC Press, 2007.

[31] J. Sunarso, S. Baumann, J.M. Serra, W.A. Meulenberg, S. Liu, Y.S. Lin, J.C.D. da Costa, Mixed ionic-electronic conducting (MIEC) ceramic-based membranes for oxygen separation, *Journal of Membrane Science*, 320 (2008) 13-41.

[32] B. Hu, K. Guo, M. Li, Y. Li, C. Xia, Effect of SDC grain size on the oxygen incorporation at the LSCF-SDC-Gas three-phase boundary, *Journal of the Electrochemical Society*, 163 (2016) F190-F195.

[33] B. Hu, Y. Wang, C. Xia, Oxygen incorporation at the three-phase boundary of LSCF-SDC composite, *Journal of Power Sources*, 269 (2014) 180-188.

[34] S. Li, J. Cheng, Y. Gan, P. Li, X. Zhang, Y. Wang, Enhancing the oxygen permeation rate of $Ba_{0.5}Sr_{0.5}Co_{0.8}Fe_{0.2}O_{3-\delta}$ membranes by surface loading Co_3O_4 nanorod catalysts, *Surface & Coatings Technology*, 276 (2015) 47-54.

[35] Y. Wang, J. Cheng, M. Huang, M. Liu, M. Li, C. Xu, Effects of surface modification with Co3O4 nanoparticles on the oxygen permeability of $Ba_{0.5}Sr_{0.5}Co_{0.8}Fe_{0.2}O_{3-\delta}$ membranes, *Applied Surface Science*, 416 (2017) 574-580.

[36] C. Yang, Q. Xu, C. Liu, J. Liu, C. Chen, W. Liu, $Bi_{1.5}Y_{0.3}Sm_{0.2}O_3$-$La_{0.8}Sr_{0.2}MnO_{3-\delta}$ dual-phase composite hollow fiber membrane for oxygen separation, *Materials Letters*, 65 (2011) 3365-3367.

[37] W. Li, J.-J. Liu, C.-S. Chen, Hollow fiber membrane of yttrium-stabilized zirconia and strontium-doped lanthanum manganite dual-phase composite for oxygen separation, *Journal of Membrane Science*, 340 (2009) 266-271.

[38] J.-j. Liu, T. Liu, W.-d. Wang, J.-f. Gao, C.-s. Chen, $Zr_{0.84}Y_{0.16}O_{1.92}$-$La_{0.8}Sr_{0.2}Cr_{0.5}Fe_{0.5}O_{3-\delta}$ dual-phase composite hollow fiber membrane targeting chemical reactor applications, *Journal of Membrane Science*, 389 (2012) 435-440.

[39] T. Liu, W. He, H. Huang, S. Wang, H.J.M. Bouwmeester, C. Chen, $Ce_{0.8}Sm_{0.2}O_{1.9}$-$La_{0.8}Sr_{0.2}Cr_{0.5}Fe_{0.5}O_{3-\delta}$ dual-phase hollow fiber membranes operated under different gradients, *Industrial & Engineering Chemistry Research*, 53 (2014) 6131-6136.

[40] T.-f. Tian, W. Li, T. Liu, C.-s. Chen, Preparation and oxygen permeability of $Ce_{0.8}Sm_{0.2}O_{2-\delta}$ - $La_{0.7}Ca_{0.3}CrO_{3-\delta}$ dual-phase composite hollow fiber membrane, *Solid State Ionics*, 225 (2012) 690-694.

[41] W. Li, T.-F. Tian, F.-Y. Shi, Y.-S. Wang, C.-S. Chen, $Ce_{0.8}Sm_{0.2}O_{2-\delta}$ -$La_{0.8}Sr_{0.2}MnO_{3-\delta}$ dual-phase composite hollow fiber membrane for oxygen separation, *Industrial & Engineering Chemistry Research*, 48 (2009) 5789-5793.

[42] S.D. Zhang, C. Li, X.X. Meng, X.Y. Tan, Z.H. Zhu, J. Sunarso, S.M. Liu, CO_2-resistant SDC-SSAF oxygen selective dual-phase hollow fiber membranes, *Asia-Pacific Journal of Chemical Engineering*, (2020) DOI: 10.1002/apj.2528.

[43] N. Han, Q. Wei, H. Tian, S. Zhang, Z. Zhu, J. Liu, S. Liu, Highly stable dual-phase membrane based on $Ce_{0.9}Gd_{0.1}O_2$-$La_2NiO_{4+\delta}$ for oxygen permeation under pure CO_2 atmosphere, *Energy Technology*, 7 (2019).

[44] M. Arnold, H.H. Wang, A. Feldhoff, Influence of CO_2 on the oxygen permeation performance and the microstructure of perovskite-type $(Ba_{0.5}Sr_{0.5})(Co_{0.8}Fe_{0.2})O_{3-\delta}$ membranes, *Journal of Membrane Science*, 293 (2007) 44-52.

[45] J.X. Yi, M. Schroeder, T. Weirich, J. Mayer, Behavior of $Ba(Co, Fe, Nb)O_{3-\delta}$ perovskite in CO_2-containing atmospheres: Degradation mechanism and materials design, *Chemistry of Materials*, 22 (2010) 6246-6253.

[46] Q. Yang, Y.S. Lin, Kinetics of carbon dioxide sorption on perovskite-type metal oxides, *Industrial & Engineering Chemistry Research*, 45 (2006) 6302-6310.

[47] J.M.D. Tascon, L.G. Tejuca, Adsorption of CO_2 on the perovskite-type oxide $LaCoO_3$, *Journal of the Chemical Society-Faraday Transactions I,* 77 (1981) 591-602.

[48] I. Arvanitidis, S.C. Du, H.Y. Sohn, S. Seetharaman, The intrinsic thermal decomposition kinetics of $SrCO_3$ by a nonisothermal technique, *Metallurgical and Materials Transactions B-Process Metallurgy and Materials Processing Science*, 28 (1997) 1063-1068.

[49] M.J. Scholten, J. Schoonman, J.C. Vanmiltenburg, H.A.J. Oonk, Synthesis of strontium and barium cerate and their reaction with carbon-dioxide, *Solid State Ionics*, 61 (1993) 83-91.

[50] G.A. ElShobaky, A.S. Ahmad, A.N. AlNoaimi, H.G. ElShobaky, Thermal decomposition of basic cobalt and copper carbonates - Thermal stability of the produced oxides as influenced by gamma-irradiation, *Journal of Thermal Analysis*, 46 (1996) 1801-1808.